Applied Thermal Engineering 221 (2023) 119862

Contents lists available at ScienceDirect

Applied Thermal Engineering

journal homepage: www.elsevier.com/locate/apthermeng

Numerical investigation of critical heat flux during subcooled flow boiling in a vertical rectangular Mini-channel

Yu-Jie Chen [a,b], Kong Ling [a], Shu-Qi Jin [a], Wei Lu [c], Bo Yu [b], Dongliang Sun [b], Wei Zhang [b], Wen-Quan Tao [a,*]

[a] *Key Laboratory of Thermo-Fluid Science and Engineering, Ministry of Education, School of Energy & Power Engineering, Xi'an Jiaotong University, Shaanxi 710049, China*

[b] *School of Mechanical Engineering, Beijing Key Laboratory of Pipeline Critical Technology and Equipment for Deepwater Oil & Gas Development, Beijing Institute of Petrochemical Technology, Beijing, 102617, China*

[c] *State Key Laboratory of Alternate Electrical Power System with Renewable Energy Sources, North China Electric Power University, Beijing 102206, China*

ARTICLE INFO

Keywords:
Critical heat flux
Flow boiling
Mini-channel
VOSET method

ABSTRACT

The critical heat flux (CHF) of flow boiling in a mini-channel is vital for equipment safety, but the boiling crisis triggering mechanism has been proved unsatisfactory. In this study, the VOSET method is adopted to investigate CHF of subcooled flow boiling in a vertical rectangular mini-channel by considering the conjugated heat transfer and using a reasonable nucleation site density model. Hundred of bubbles are accurately captured, and the evolutions of flow pattern, dry patch, and wall superheating are reproduced. Based on those, the relationship between boiling crisis and dry patch is demonstrated. When the heat flux is lower, some middle-sized isolated bubbles adhere to the wall surface with a dry patch below. This dry patch can be rewetted quickly. Hence, the wall superheating increases slightly along the flow direction and is within control. With the increasing heat flux, the dry patch expands because some big bubbles merge into the elongated bubble, leading to the local heat transfer deterioration, but the local wall superheating rise is still limited due to heat conduction inside the solid wall and the rewetting effect. However, the continuous coalescence of elongated bubbles midstream and downstream causes the appearance of an almost permanent dry patch with a high local wall superheating of 183.04 K near the outlet of the mini-channel when the heat flux rises to 500 kW/m^2, which has exceeded the CHF of 375 kW/m^2 obtained in this study. This triggering mechanism of the flow boiling crisis is new and different from the traditional ones. Besides, the departure from nucleate boiling (DNB) is found at 325 kW/m^2, beyond which the wall superheating increases rapidly with heat flux.

1. Introduction

Compared with the heat transfer of single-phase flow, that of flow boiling has the advantages of high heat transfer coefficient (HTC) and lower wall superheating. Therefore, it has a wide range of applications in the nuclear industry, advanced electronic devices, aerospace, and other fields [1,2]. CHF of the flow boiling in the mini-channel is vital for the operation safety of compact equipment, and to this end, many significant works have been done [2–8]. But the so-far proposed triggering mechanism of boiling crisis (when heat flux exceeds CHF) has been proved unsatisfactory.

Tong [3] correlated the experimental CHF data by using the concept of boundary-layer separation. The flow boiling crisis began with the quick evaporation of stagnant liquid under the boundary layer. Weisman and Pei [4] presented a theoretical prediction model of CHF for high-velocity flow based on the fluid interchange between the core region and the bubbly layer. The CHF appeared when the liquid transport between the bubbly layer and core was limited. Lee and Mudawwar [5] developed a sublayer dry-out model to predict CHF during vertical subcooled flow at high pressure and high mass velocity. Flow boiling crisis happened when a thin liquid layer beneath an intermittent vapor blanket dried out because of Helmholtz instability at the sublayer-vapor interface. Galloway and Mudawar [6] proposed an interface separation model based on the wavy distribution of the vapor–liquid interface near the wall. Only the trough of the wavy vapor–liquid interface could wet the heating wall. While the vapor–liquid interface would be pushed away from the heating wall if the heat flux was large enough, resulting in

---

* Corresponding author.
E-mail address: wqtao@mail.xjtu.edu.cn (W.-Q. Tao).

https://doi.org/10.1016/j.applthermaleng.2022.119862
Received 17 June 2022; Received in revised form 19 October 2022; Accepted 9 December 2022

Nomenclature

A	Liquid-vapor interface area, m^2
B	Exponent in the nucleation site density model
c	Heat capacity, J/(kg·K)
C	Exponent in the nucleation site density model
$C(p)$	Empirical parameter depending on the pressure
D	Characteristic diameter, m
$\mathbf{f}$	Surface tension, N/m^3
F	Reynolds number factor
$\mathbf{g}$	Gravitational acceleration, m/s^2
G	Mass flux, kg/(m^2•s)
h	Latent heat, J/kg
$h_{local,ave}$	Local heat transfer coefficient of the wall, W/(m^2•K)
h_{nb}	Heat transfer coefficient of nucleate pool boiling
h_{tp}	Heat transfer coefficient of flow boiling, W/(m^2•K)
$h_{w,ave}$	Average heat transfer coefficient of the wall, W/(m^2•K)
$h_{sp,l}$	Heat transfer coefficient of single-phase flow, W/(m^2•K)
$\dot{m}$	Phase change rate, kg/(m^3•s)
M	Molecular mass, kg/kmol
N	Total wall surface nodes
N_0	Coefficient of nucleation site density model, site/m^2
p	Pressure, Pa
P_R	Relative pressure to critical pressure
q	Heat flux of heating wall, W/m^2
$\dot{q}$	Heat flux of phase transition, W/m^2
q_i	Heat flux of ith wall surface node, W/m^2
S	Suppression factor
t	Time, s
Δt	Time interval, s
T	Temperature, K
T_0	Temperature constant in nucleation site density model, K
T_b	Fluid temperature, K
$T_{b,ave}$	Average fluid temperature, K
$T_{b,local}$	Local fluid temperature, K
T_c	Critical temperature of water, K
T_w	Wall temperature, K
$T_{w,ave}$	Average temperature of the whole wall surface, K
$T_{w,local}$	Average temperature of the local wall surface, K
T_{sat}	Saturated temperature, K
ΔT_{sup}	Wall superheating, K
$\Delta T_{sup,w}$	Spatial average superheating of the whole wall surface, K
$\Delta T_{sup,w,ave}$	Temporal-spatial average superheating of the whole wall surface in the dynamically stable stage of flow boiling, K
$\Delta T_{sup,l,ave}$	Temporal-spatial average superheating of the local wall surface in the dynamically stable stage of flow boiling, K
ΔT_{sub}	Subcooling, K
$\mathbf{u}$	Velocity vector, m/s
v_{inlet}	Inlet velocity, m/s
V	Control volume, m^3
x	Vapor fraction

Greek letters

γ	Exponent in contact angle model
η	Dynamic viscosity, Pa•s
η_t	Turbulent viscosity, Pa•s
θ_0	Contact angle constant in nucleation site density model, °
λ	Thermal conductivity, W/(m·K)
ρ	Density, kg/m3
ψ	Enhancement factor

Non-dimensional numbers

Bo	Boiling number
Ja	Jacobi number
Nu_{tp}	Nusselt number of flow boiling
Nu_{sp}	Nusselt number of single-phase flow
Pr	Prandtl number
Pr_t	Turbulent Prandtl number
Re	Reynolds number

Subscripts

ave	Average value
b	Bulk
c	Critical
inlet	Inlet of channel
l	Liquid
local	Local value
nb	Pool boiling
R	Relative value
s	Solid
sat	Saturation
sp	Single phase
tp	Flow boiling
v	Vapor
w	Wall
sup	Superheating
sub	Subcooling

Acronyms and abbreviations

2D	Two-dimensional
3D	Three-dimensional
AMG	Algebraic multigrid
CFD	Computational fluid dynamics
CHF	Critical heat flux
DNB	Departure from nucleate boiling point
HTC	Heat transfer coefficient
LS	Level set
PWR	Pressurized water reactor
VOF	Volume of fluid
VOSET	Coupled volume-of-fluid and level set

the boiling crisis. Liu and Nariai [7] investigated boiling crisis triggering mechanism based on the homogeneous nucleation. A significant number of homogeneous vapor bubbles generated and accumulated near the wall, triggering the boiling crisis. Ha and No [8] proposed a new dry-spot model to predict CHF in pool boiling and forced convection boiling. A dry patch appeared when many bubbles formed around one bubble and restricted the liquid feeding this bubble. With the increase in the number and size of the dry patches, the number of effective nucleation sites diminished, leading to the boiling crisis. Kim et al. [9] conducted a visual study of DNB during a vertical upward flow boiling. It was found that the isolated bubble flow turned into an elongated bubble flow with the increasing heat flux. The evaporation of the thin liquid film below the elongated bubble caused a periodic dry patch formation. And an irreversible dry patch appeared with increased heat flux further, leading to the departure from nucleate boiling. Hata et al.[10] investigated the subcooled boiling heat transfer in a vertical tube with high mass fluxes. A comparison was performed between experimental results and theoretical results obtained by the sublayer liquid dry-out model. Besides, different dominant mechanisms for the boiling crisis at high liquid Reynolds numbers were discussed in detail. It is worth stressing that most of the above models are proposed based on the macro channel, and their availability in the mini-channel is still unknown.

In this paper, the focus will be paid to the flow boiling in the mini-channel. The numerical simulation method can obtain detailed information during the flow boiling, which favors revealing the triggering mechanism of the boiling crisis in the mini-channel. However, few works about CHF of flow boiling have been reported. Sato and Niceno [11] numerically studied pool boiling using a color function to capture the liquid–vapor interface. The boiling patterns covered from the nucleate boiling to the film boiling, and a CHF of 1200 kW/m^2 was obtained in their study. DolatiAsl et al. [12] investigated the CHF during the subcooled flow boiling of water–alumina nanofluid based on the Euler–Euler model under different fluid subcooling, mass fluxes, tube angles, and nanoparticle volumes. The CHF was obtained based on whether the sudden change of wall surface temperature happened along the flow direction. However, the conjugated heat transfer between solid wall and fluid was neglected in their study. Zhang et al. [13] adopted the Eulerian two-fluid model to predict the CHF under pressurized water reactor (PWR) conditions, and the effects of secondary flow on CHF were explored. But the accurate two-phase interface was neglected, which was detrimental to revealing the intrinsic mechanism of the boiling crisis. Pothukuchi et al. [14] reviewed CFD modeling of CHF in flow boiling. The model availability in predicting wall superheating and CHF was assessed, while the triggering mechanism of boiling crisis was not the concern. In summary, the reported numerical simulation works are far from enough to reveal the triggering mechanism of CHF during the flow boiling in a mini-channel, and the main reasons are characteristic size difference and neglect of /less attention is paid to the accurate interface capture.

At present, based on interface capture methods, including Level-set [15], VOF [16], and VOSET [17], many related numerical simulation studies focusing on bubble behaviors in flow boiling have been done. Mukherjee and Kandlikar [18,19] analyzed the growth of a single bubble in a three-dimensional (3D) microchannel using the Level-set method. A trapped liquid layer was observed below the bubble as it elongated, and a dry patch was found when the elongated bubble filled the channel. Besides, the hydrophilic wall could retard the formation of the dry patch and enhance heat transfer. Lee and Son [20] adopted the Level-set method to investigate the subcooled flow boiling in a mini-channel by considering the conjugated heat transfer. The flow and heat transfer characteristics during the growth and coalescence of several bubbles were illustrated. Lee et al. [21] employed the Level-set method to thoroughly investigate the effects of fin height, spacing, and length on the flow boiling in a finned microchannel. However, only one or two elongated bubbles were captured. Zu et al. [22] used the VOF method to study the velocity, temperature, and pressure fields of bubbly flow generated by a vapor inlet on the sidewall. Luo et al. [23] adopted the VOF method to explore the effects of inlet mass flux, wall heat flux, and inlet vapor quality on heat transfer in a 3D annular flow. Ling et al. [24] conducted the VOSET method to analyze the growth and coalescence of bubbles in a 3D microchannel. And recently, Ling et al. [25] discussed bubble activities and flow patterns of two-dimensional (2D) subcooled flow boiling at different fluxes in detail. The above numerical studies have provided significant insights into the flow boiling in the mini-channel. However, most of them only include several bubbles because of the computation cost or model limitation, and some neglect the conjugated heat transfer. These deficiencies hinder the study of heat flux effects on wall superheating and flow patterns, leading to the difficulty in revealing the triggering mechanism of boiling crisis during the flow boiling further.

Therefore, in this study, based on a nucleation site density model obtained by the experimental method, the VOSET method reconciling both efficiency and accuracy is adopted to study the triggering mechanism of boiling crisis during the subcooled flow boiling in a vertical rectangular 3D mini-channel by considering the conjugated heat transfer. The evolution of wall superheating with bubble activities, flow pattern, and the dry patch is discussed thoroughly under different heat fluxes for the auxiliary analysis of the triggering mechanism of boiling crisis.

2. Problem description

As shown in Fig. 1, the subcooled flow boiling in a vertical rectangular mini-channel with a size of 1.0 mm (x) × 1.0 mm (y) × 20.0 mm (z) is investigated to reveal the flow boiling crisis. The water with a subcooling of 20 K ($\Delta T_{sub} = T_{sat} - T_{inlet}$) gets into the channel from the bottom inlet at 0.1 m/s. The solid wall with a thickness of 0.2 mm on the right side of the channel is adopted to consider the conjugated heat transfer, and the heat flux varying from 200 kW/m^2 to 500 kW/m^2 is added to the outside of the wall. The other surrounding sides perpendicular to the z-direction are no-slip and adiabatic walls (Table 1).

The heating wall is monocrystal silicon with thermal conductivity of 148 W/(m·K), and the static contact angle of a water droplet on that is set as 50°. The system pressure is 1 MPa, corresponding to saturated temperature and latent heat of 453 K and 2.02 × 10^6 J/kg, respectively. Liquid-vapor surface tension is 0.042 N/m. The other physical properties are listed in Tab. 1.

3. Mathematical models

3.1. Governing equations

As shown in Fig. 1, the computation region includes the solid and fluid regions. The unsteady heat conduction in the solid region is described by Eq. (1).

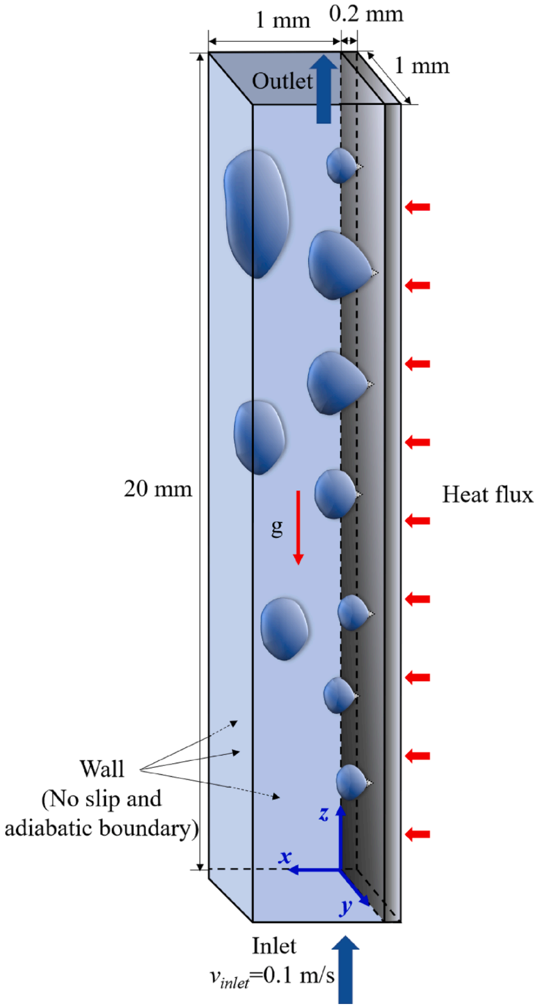

Fig. 1. Configurations of 3D vertical rectangular mini-channel.

Table 1

Physical properties of study mediums.

	Density (kg/m^3)	Viscosity (Pa·s)	Thermal conductivity (W/(m·K))	Heat capacity (J/(kg·K))
Wall	2330	–	148	766
Liquid	888.1	1.51×10^{-4}	0.674	4400
Vapor	5.14	1.5×10^{-5}	0.036	2712

$$\frac{\partial(\rho_s c_s T)}{\partial t} = \nabla\cdot(\lambda_s \nabla T) \tag{1}$$

where ρ is the density, kg/m^3; c is the heat capacity, J/(kg·K); λ is the thermal conductivity, W/(m·K), T is the temperature, K.

In this study, two assumptions are made for the numerical simulation in the fluid region: the fluid is incompressible; the liquid–vapor interface temperature is set as the saturated temperature [25]. Based on those, the flow, heat transfer, and phase transition in the fluid region are described by Eqs. (2)-(7).

$$\nabla\cdot\mathbf{u} = \left(\frac{1}{\rho_v} - \frac{1}{\rho_l}\right)\dot{m} \tag{2}$$

$$\frac{\partial(\rho\mathbf{u})}{\partial t} + \nabla\cdot(\rho\mathbf{u}\mathbf{u}) = -\nabla p + \nabla\cdot\left[(\eta+\eta_t)\left(\nabla\mathbf{u} + \nabla\mathbf{u}^T\right)\right] + \mathbf{f} + \rho\mathbf{g} \tag{3}$$

$$\frac{\partial\left(\rho_l c_{p,l} T\right)}{\partial t} + \nabla\cdot\left(\rho_l c_{p,l}\boldsymbol{u}T\right) = \nabla\cdot\left[\left(\lambda_l + \frac{c_{p,l}\mu_t}{Pr_t}\right)\nabla T\right] \tag{4}$$

$$\frac{\partial\left(\rho_v c_{p,v} T\right)}{\partial t} + \nabla\cdot\left(\rho_l c_{p,v}\boldsymbol{u}T\right) = \nabla\cdot\left[\left(\lambda_l + \frac{c_{p,v}\mu_t}{Pr_t}\right)\nabla T\right] \tag{5}$$

$$\int_V \dot{m}\,\mathrm{dV} = \frac{1}{h}\int_A \dot{q}\,\mathrm{dA} \tag{6}$$

$$\dot{q} = \lambda_v \left.\frac{\partial T}{\partial n}\right|_v - \lambda_l \left.\frac{\partial T}{\partial n}\right|_l \tag{7}$$

where $\mathbf{u}$ is the velocity vector, m/s; $\dot{m}$ is the phase change rate, kg/(m^3•s); η is the dynamic viscosity, Pa•s; η_t is the turbulent viscosity calculated by the Smagorinsky model [26], Pa•s; $\mathbf{f}$ is the surface tension calculated by the CSF model [27], N/m^3; $\mathbf{g}$ is the gravity, m/s^2; Pr$_t$ is the turbulent Prandtl number; h is the latent heat of water, J/kg; $\dot{q}$ is the heat flux caused by phase transition[28], W/m^2; the indexes s, l, and v represent the phase of solid, liquid, and vapor, respectively.

In this study, the vapor–liquid interface is captured by the VOSET method [17], which possesses the advantage of both VOF and Level-set methods with less computational cost. The implemented details of the 3D VOSET method can refer to Ref. [29]. The boundary conditions of the computational domain are set as follows. The constant temperature and velocity boundaries are applied at the channel inlet; the free outlet boundary is used at the channel outlet; the no-slip boundary is employed for all walls; a constant heat flux is applied to the outer surface of the right heating wall, and the other walls are adiabatic boundaries.

The finite volume method (FVM) is conducted to discretize Eqs. (1)-(7) and boundary conditions, and the discrete equations are solved by the efficient algebraic multigrid (AMG) method. The projection algorithm is adopted to deal with the coupling between pressure and velocity. The solving of the abovementioned variables and the control of solving procedure are completed by a self-programming code.

3.2. Nucleation model

Bubble nucleation is one of the most challenging issues for the macro numerical simulation of flow boiling, and in the present study, it is described by a nucleation site density model developed from theoretical analysis and experimental data. The system pressure of 1.0 MPa in this study is high, which can not be handled by common nucleation site density models. After a literature search, the model developed by Li et al. [30] is adopted to determine the active nucleation site density, which has been verified by experimental data under a wide range of pressure: 0.101 MPa–19.8 MPa. This model consists of Eqs. (8)-(12), where the active nucleation site density is related to the wall superheating, pressure, and contact angle. In this study, the pressure and contact angle are constant, and the active nucleation site is only decided by the wall superheating.

$$N_w = N_0(1-\cos\theta)\exp[f(p)]\Delta T_{sup}^{C\Delta T_{sup}+B} \tag{8}$$

$$f(p) = 26.006 - 3.678\exp(-2p) - 21.907\exp\left(-\frac{p}{24.065}\right) \tag{9}$$

$$C = -0.0002p^2 + 0.0108p + 0.0119 \tag{10}$$

$$B = 0.122p + 1.988 \tag{11}$$

$$1-\cos\theta = (1-\cos\theta_0)\left(\frac{T_c - T_{sat}}{T_c - T_0}\right)^{\gamma} \tag{12}$$

where $N_0 = 1000$ site/m^2, $\theta_0 = 41.37^{\circ}$, $T_c = 374\,^{\circ}\mathrm{C}$, $T_0 = 25\,^{\circ}\mathrm{C}$, $\gamma = 0.719$ by default [30]. The unit of the pressure p is MPa.

In implementing the nucleation model, the activated nucleation site number for a special condition is determined by the nucleation site density first; then, the preset nucleation sites are randomly put on the inner side of the heating wall. Once one nucleation site reaches its predetermined nucleation conditions, an artificial bubble nucleus with a radius of one grid is put there. From this implementation process, it is clear that the abovementioned nucleation model will fail without considering the conjugated heat transfer.

3.3. Models verification

In this study, the uniform cubic grid is adopted to discretize the fluid region. The fluid mesh is consistent with solid mesh at the fluid–solid interface, and a fine grid spacing of 20 μm is applied to discretize the solid wall along the x-direction. In the grid-independence study, average wall superheating of 15.02 and 14.48 K are obtained in the dynamically stable stage of flow boiling based on the fluid meshes with uniform 312,500 nodes and 439,040 nodes under the heat flux of 250 kW/m^2. The relative difference is 3.60 %, which is acceptable considering the high computation cost, different nucleation site distributions in different grids, and the complexity of the two-phase heat transfer problem. Therefore, the grid with a total node of 437500, including 312,500 fluid and 125,000 solid nodes, is employed in this study to conduct the numerical simulations.

The common correlations of flow boiling obtained by experimental data can be classified into four categories: enhancement-factor, superposition, asymptotic,$q \sim \Delta T_{sat}^n$, and flow pattern-based types[2]. Next, comparisons are made with some representative correlations for subcooled flow boiling heat transfer to validate numerically predicted results in this study.

Shah correlation (enhancement-factor model) [31]

$$q = h_{tp}(T_w - T_{sat}) = \psi h_{sp,l}(T_w - T_{sat}) \tag{13}$$

$$h_{sp,l} = 0.023Re_l^{0.8}Pr_l^{0.4}\frac{\lambda}{D} \tag{14}$$

$$\psi = \begin{cases} \psi_0 \text{ for low subcooling} \\ \psi_0 + (T_{sat} - T_b)/(T_w - T_{sat}) \text{ for high subcooling} \end{cases} \tag{15}$$

$$\psi_0 = \begin{cases} 230\mathrm{Bo}^{0.5} \text{ for } \mathrm{Bo} > 0.3\times10^{-4} \\ 1 + 46\mathrm{Bo}^{0.5} \text{ for } \mathrm{Bo} < 0.3\times10^{-4} \end{cases} \tag{16}$$

$$\mathrm{Bo} = \frac{\mathrm{q}}{\mathrm{Gh}} \tag{17}$$

where h_{tp} and $h_{sp,l}$ represent the HTC of flow boiling and single-phase flow, respectively, and the latter is calculated by Dittus–Boelter correlation [32] (Eq. (14)), W/(m^2•K); Re is the Reynolds number; Pr is the Prandtl number; D is the characteristic diameter, m; ψ is the enhancement factor calculated by Eqs. (15)~(17); Bo is the boiling number; G is the mass flux, kg/(m^2•s).

Papell correlation (enhancement-factor model) [33]

$$\frac{\mathrm{Nu_{tp}}}{\mathrm{Nu_{sp}}} = 90.0\mathrm{Ja}^{-0.84}\left(\frac{\mathrm{q}}{\mathrm{h}\rho_{\mathrm{g}}\mathrm{u}}\right)^{0.7}\left(\frac{\rho_{\mathrm{g}}}{\rho_{\mathrm{l}}}\right)^{0.7} \tag{18}$$

$$\mathrm{Nu_{sp}} = 0.021\mathrm{Re_l^{0.8}Pr_l^{0.4}} \tag{19}$$

$$\mathrm{Ja} = \frac{\mathrm{c_{p,l}}\Delta\mathrm{T_{sub}}}{\mathrm{h}} \tag{20}$$

where $\mathrm{Nu_{tp}}$ and $\mathrm{Nu_{sp}}$ express the Nusselt number of flow boiling and single-phase flow, respectively; Ja is the Jacobi number calculated by Eq. (20); $\Delta T_{sub} = T_{sat} - T_b$ is the fluid subcooling, K; T_b is the fluid temperature, K.

Gungor–Winterton correlation (superposition model)[34]

$$q = h_{sp,l}(T_w - T_b) + Sh_{nb}(T_w - T_{sat}) \tag{21}$$

$$h_{nb} = 55P_R^{0.12}(-0.4343\ln P_R)^{-0.55}M^{-0.5}q^{0.67} \tag{22}$$

$$S = 1/\left(1 + 1.15\times10^{-6}F^2Re_l^{1.17}\right) \tag{23}$$

$$F = 1 + 2.4\times10^4\mathrm{Bo}^{1.16} \tag{24}$$

where h_{nb} is the HTC of nucleate pool boiling calculated by Cooper equation [35] (Eq. (22)), W/(m^2•K); S is the suppression factor; F is the Reynolds number factor; P_R is the relative pressure to critical pressure; M is the molecular mass, kg/kmol.

Liu-Winterton correlation (asymptotic model)[36]

$$q^2 = \left[Fq_{sp,l}\right]^2 + (Sq_{nb})^2 = \left[Fh_{sp,l}(\Delta T_{sat} + \Delta T_{sub})\right]^2 + (Sh_{nb}\Delta T_{sat})^2 \tag{25}$$

$$S = 1/\left(1 + 0.55F^{0.1}Re_l^{0.16}\right) \tag{26}$$

$$F = \left[1 + xPr_l\left(\rho_l/\rho_g - 1\right)\right]^{0.35} \tag{27}$$

where x is the vapor fraction.

Kutateladze correlation (asymptotic model)[37]

$$h_{tp}^2 = h_{sp,l}^2 + h_{nb}^2 \tag{28}$$

$$h_{nb} = C(p)q^{0.7} \tag{29}$$

$$q = h_{tp}(T_w - T_{sat}) \tag{30}$$

where $C(p)$ is an empirical parameter depending on the pressure, and how to obtain its value can refer to Ref. [37].

Fig. 2 displays the average wall superheating calculated by experimental correlations and numerical methods under different heat fluxes. The results indicate that the changing trend of predicted results is similar to empirical correlations, especially the Gungor-Winterron correlation. Table 2 lists the relative differences between numerically predicted results and different correlations. Quantitatively, regarding the numerically predicted results, there is a maximal average relative difference of 37.99 % compared with the Papell correlation, and a minimum of 10.00 % is obtained compared with the Liu-Winterton correlation.

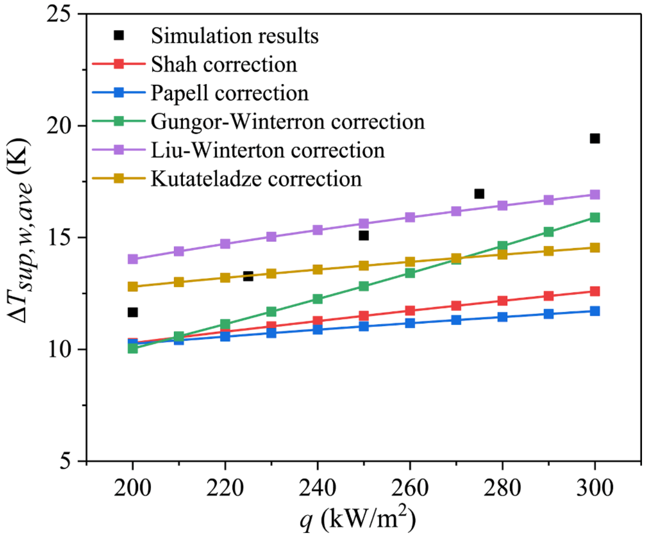

Fig. 2. Comparisons in average wall superheating between experimental correlations and numerical methods under different heat fluxes.

It is well-known in the heat transfer textbook [32] that the Rohsenow equation for pool boiling heat transfer can have a 30 % margin of error for a wall superheating by a given heat flux. The maximum relative differences in predicted results of wall superheating between the present numerical simulation and the Gungor–Winterton and Liu-Winterton correlations are less than 25 %, which is acceptable.

4. Simulation results and discussion

In this section, the flow pattern and heat transfer of the subcooled flow boiling in a vertical mini-channel with different heat fluxes are demonstrated, and the triggering mechanism of CHF is revealed.

4.1. The evolution of wall superheating with flow patterns under different heat fluxes

The evolution of wall superheating with flow patterns is one of the most intuitive ways to observe the CHF phenomenon. Hence it is firstly presented in this subsection.

Fig. 3 illustrates the representative snapshots of the subcooled flow boiling under different heat fluxes. Light blue and white colors represent liquid and liquid–vapor interface, respectively; the wall superheating decides the wall color. It is worth stressing that the presented temperature in this paper is the wall superheating. Once the heat flux is added outside the heating wall, the liquid is heated by the conjugated heat transfer. When the liquid and wall reach a certain temperature, the phase transition ensues with some activated bubbles. Under different heat fluxes, different numbers of bubbles are activated because of different wall superheating, leading to visibly different flow patterns of flow boiling. Furthermore, the wall superheating changes with the evolution of flow patterns. Next, the developments of flow patterns and wall superheating are demonstrated in detail.

As shown in Fig. 3(a), when the heat flux is 200 kW/m^2, the wall superheating is low in the initial stage, and only a few bubbles are activated. As time goes on, more and more bubbles are activated, and these bubbles grow and merge into a big one or condense and shrink inside the subcooled liquid. After 200 ms, the flow pattern is stable. The bubble size is smaller than the characteristic size of the mini-channel, and only bubbly flow happens at this heat flux. Under the effect of bubbly flow, the wall superheating is still at a low level. It is noteworthy

Table 2
Relative differences between present simulation results and different correlations.

Relative difference(%)	Shah correlation	Papell correlation	Gungor–Winterton correlation	Liu-Winterton correlation	Kutateladze correlation
Maximum	54.20	65.87	22.21	16.95	33.54
Minimum	13.32	13.77	16.10	3.45	0.20
Average	32.17	37.99	18.14	10.00	14.45

that a small dry patch appears below the middle-size bubble, but there will be quickly rewetted without significant local temperature rise. Therefore, there is no significant difference in the wall superheating along the flow direction, and a more detailed quantitative comparison will be provided in the next section.

When the heat flux increases to 300 kW/m^2, as shown in Fig. 3(b), the activated bubble number is larger than that in the case with the heat flux of 200 kW/m^2 at the same time step. Many small bubbles coalesce into a big one close to the mini-channel's characteristic size. At 50 ms, it can be observed that the wall superheating of the nucleate boiling region is lower than that in the single-phase flow region. At 200 ms, a slightly elongated bubble is observed at the outlet of the mini-channel, and the dry patch area below expands. Moreover, a slight wall superheating increase is found in this dry patch region. Fortunately, few elongated bubbles are observed with time, and the slightly larger dry patch is still rewetted quickly by the subcooled liquid. Besides, because of the high thermal conductivity of the solid wall, some heat from the dry patch region will be conducted to the first half of the mini-channel and brought away by the fluid. Therefore, the whole wall superheating is still low when the heat flux is 300 kW/m^2. Only bubbly flow happens in the mini-channel, with the wall superheating increasing slightly along the flow direction. The CHF has not been triggered yet.

As shown in Fig. 3(c), as the heat flux rises to 400 kW/m^2, many bubbles are activated and quickly merge into some big bubbles. Still, the flow pattern is bubbly flow before 100 ms, and the wall superheating does not change much along the flow direction because of the bubble activities and wall conduction. However, after 200 ms, these big bubbles cannot leave away from the mini-channel and only coalesce into elongated bubbles in the second half of the mini-channel. The flow pattern changes into the slug flow from the bubbly flow along the flow direction. A long dry patch appears below the elongated bubble, and the hot wall directly exchanges the heat with the vapor. The wall superheating of the dry patch region rises more quickly than the other regions covered by subcooled liquids. Even the liquid in the bottom corner of the mini-channel section is almost dried out. Unfortunately, the dry patch needs some time to be rewetted again. As a result, the local wall superheating of the dry patch region near the channel outlet keeps growing to a high value of 110.46 K, leading to the local heat transfer deterioration when the heating time is over 300 ms.

As the heat flux increases to 500 kW/m^2, 138 bubbles are accurately captured at the instant of 35 ms, which is the most bubble number in the present study. These small bubbles merge into an elongated one in a short time. A dry patch with a half-pipe length appears after 200 ms, and the elongated bubble needs more time to get out of the mini-channel. Besides, as shown in Fig. 4, an elongated bubble in the middle of the channel merges into the downstream one, hindering the rewetting of the dry patch near the outlet and causing a significant wall superheating increase. The ratio of rewetting time to monopolized time of the dry patch near the outlet is very small, and the dry patch there almost becomes permanent, as shown in Fig. 3(d). As a result, heat transfer deterioration in the channel outlet happens rapidly, with the local wall superheating increasing to the highest value of 183.04 K in this study. The wall superheating of over 110 K is intolerable when heat flux exceeds 400 kW/m^2, and it can be considered that the boiling crisis has happened due to prolonged local dry. It is noteworthy that the main content to illustrate in this subsection is why the wall superheating increases to an extremely high value with increasing heat flux, that is, the intrinsic triggering mechanism of the flow boiling crisis. Whether the applied heat flux has exceeded CHF needs a quantitative criterion, which will be provided by wall superheating profiles in the next section. In addition, unlike the pool boiling, the elongated bubble will be pushed out of the mini-channel, and the dry patch will be rewetted sooner or later for the slug flow. Moreover, some heat of the dry patch region is brought away by vertical heat conduction of the wall, which will also be quantitatively explained in the next section. Therefore, the local wall superheating will change periodically and won't be totally out of control when the boiling crisis appears.

The present simulation results are similar to the theories presented by Lee and Mudawwar [5] and Ha and No [8], namely, the formation and development of dry patches below the bubble trigger flow boiling crisis. However, the reason for the formation and development of dry patches is different, and the cause in this study is the appearance of the elongated bubble, which is similar to the experimental results of Kim et al. [9].

In summary, different flow patterns of subcooled flow boiling happen in the mini-channel under different heat fluxes, significantly affecting the heat exchange between the heating wall and fluid. The wall superheating is almost homogeneous when only bubbly flow happens. Whereas, once the flow pattern turns into slug flow, a distinct hot spot occurs on the heating wall due to the formation of dry patches. Furthermore, a significant wall superheating increase happens with the appearance of an almost permanent dry patch near the outlet, triggering the boiling crisis.

4.2. *Quantitative analysis of heat transfer characteristic of subcooled flow boiling in a vertical mini-channel under different heat fluxes*

In this subsection, a quantitative analysis of heat transfer characteristics of subcooled flow boiling in a vertical mini-channel under different heat fluxes is presented, and values of ONB and CHF are provided.

4.2.1. *Quantitative analysis of whole wall heat transfer characteristics*

Firstly, a quantitative analysis of whole wall heat transfer is made. Fig. 5 illustrates the trends of average wall superheating under the representative heat fluxes. When a constant heat flux is added to the outside wall, the wall superheating increases and reaches a dynamically stable value after about 400 ms for all cases. During the dynamically stable stage, the wall superheating oscillates with the bubble activities. When the heat flux is 500 kW/m^2, the amplitude is distinct because of the evolution of the long dry patch, with a value of about 15 K, as shown in Fig. 3(d). The temporal-spatial average wall superheating during the stable stage under the heat fluxes of 200, 300, 400, and 500 kW/m^2 are 11.66, 19.42, 43.70, and 77.26 K, respectively. The wall superheating rises with the increase of heat flux. It is worth stressing that the statistics in the following parts are based on the data in the dynamically stable stage.

The average temperature of the fluid is adopted as the reference temperature for calculating the temporal-spatial average HTC based on the Newton's law of cooling, as displayed in Eq. (31). Fig. 6 demonstrates the trends of temporal-spatial average wall superheating and HTC under representative heat fluxes. The wall superheating increases with the heat flux, while the HTC increases firstly and then decreases. It can be found that under high heat flux conditions, although the nucleate boiling intensity increases upstream, the dry patch develops downstream, leading to the reduction of the overall HTC. Moreover, when the

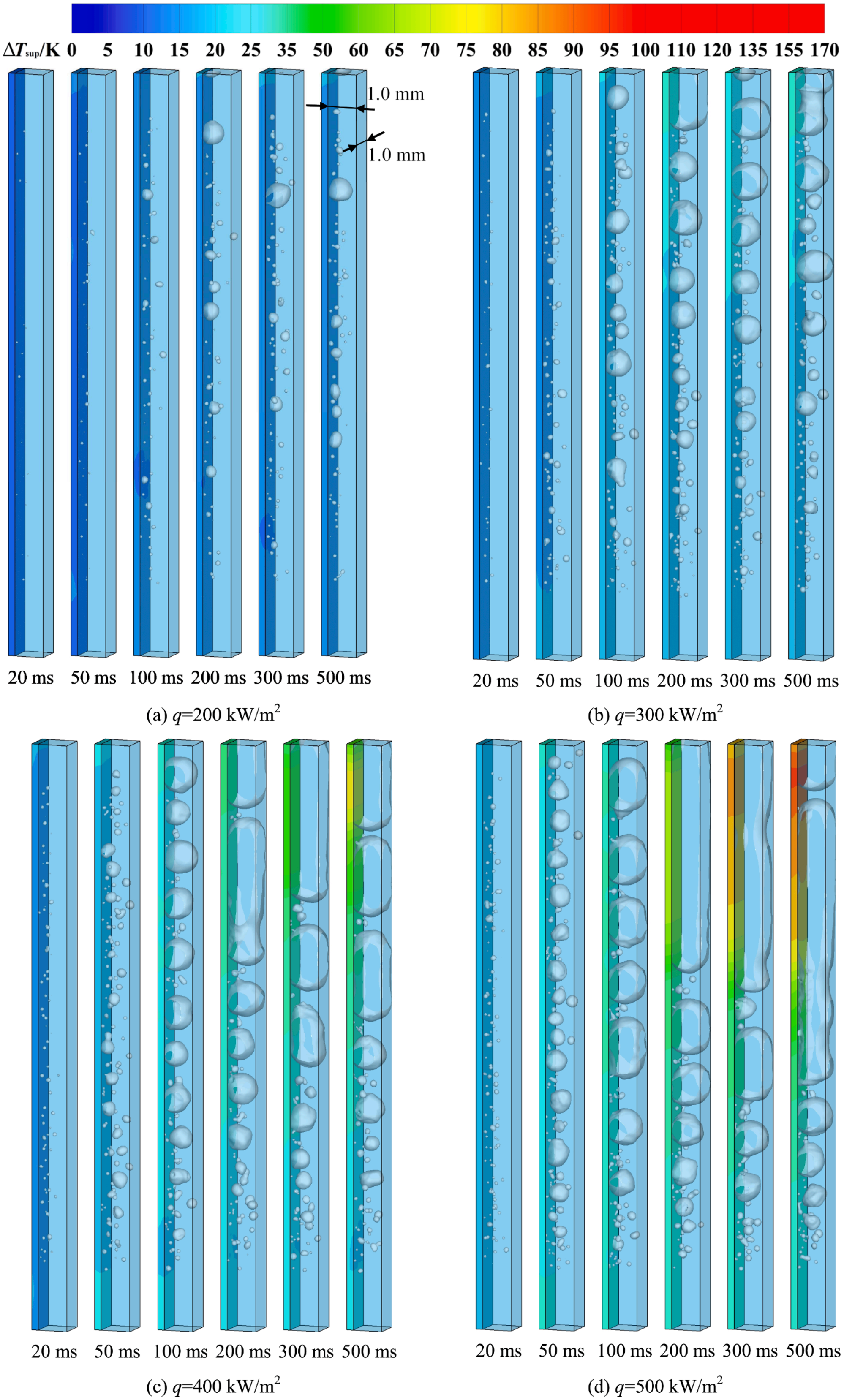

(a) q=200 kW/m^2 (b) q=300 kW/m^2

(c) q=400 kW/m^2 (d) q=500 kW/m^2

Fig. 3. Representative snapshots of 3D subcooled flow boiling under different heat fluxes.

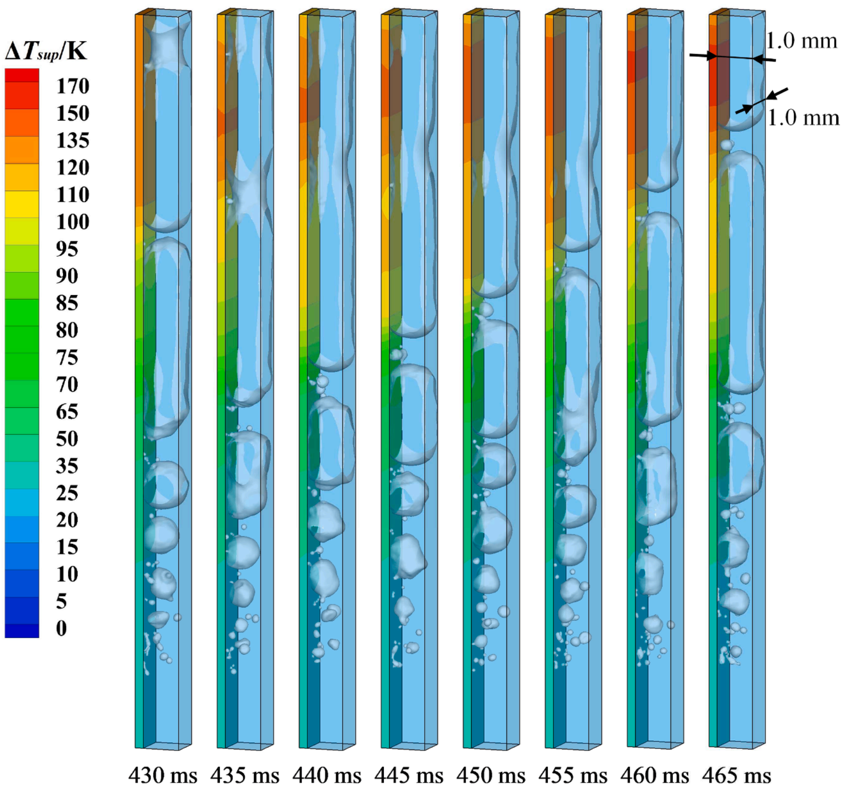

Fig. 4. Representative snapshots of elongated bubble coalescence and wall superheating rise when the heat flux is 500 kW/m^2.

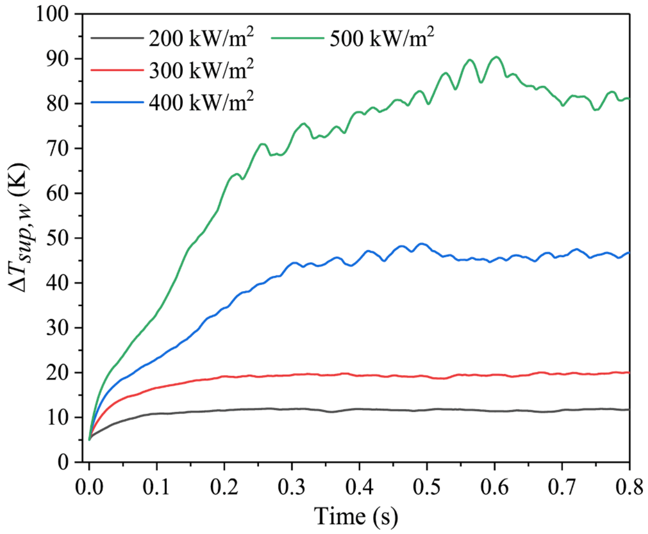

Fig. 5. Trends of spatial average heating wall superheating under representative heat fluxes.

heat flux is 500 kW/m^2, the HTC is only 57.2 % of the maximum value obtained at 275 kW/m^2, thus, the wall superheating rises rapidly, causing the boiling crisis.

$$h_{w,ave} = \sum_{t}^{t+\Delta t} \frac{\sum_i^N q_i/N}{\left(T_{w,ave} - T_{b,ave}\right)}/\Delta t \tag{31}$$

where q_i is the heat flux of ith wall surface node; N is the total wall surface nodes.

On the other hand, the changes of temporal-spatial average wall superheating and HTC can be divided into three stages within the studied heat flux range. Before reaching 275 kW/m^2, the flow pattern is bubbly flow, which is the first stage, as shown in Fig. 3(a). With the heat flux increasing, the wall superheating rises slowly, but HTC improves rapidly. After that, the flow pattern tends to turn into or has become slug flow in the second half of the mini-channel from 275 to 400 kW/m^2, which is the second stage, as shown in Figs. 3 (b) and (c). A clear dry patch appears below the elongated bubble, leading to the quick increase of wall superheating while a rapid decrease of HTC. The dry patch area broadens with the heat flux, and the wall superheating and HTC curves behave at a contrary trend. While the heat flux is over 400 kW/m^2 to the third stage, the slug flow region and dry patch area expand. Wall superheating and HTC continue to increase and decrease, respectively, but the change rate reduces. The reasons for the changing trend of wall superheating and HTC at the first and second stages have been illustrated before, so that won't be covered again here. Next, an additional explanation is made for the third stage. As shown in Fig. 7, the wall

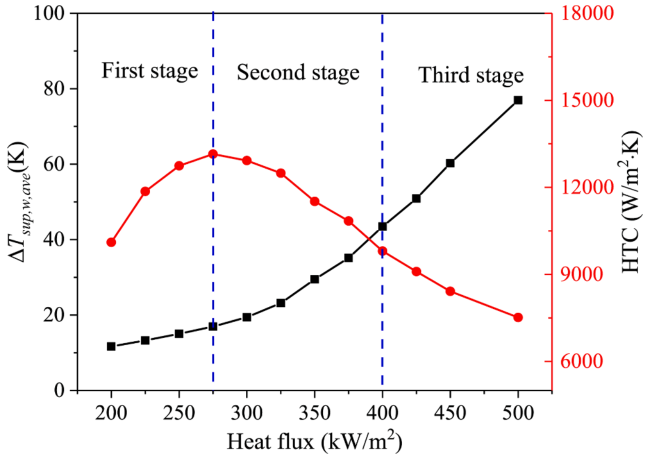

Fig. 6. Profiles of temporal-spatial average wall superheating and HTC.

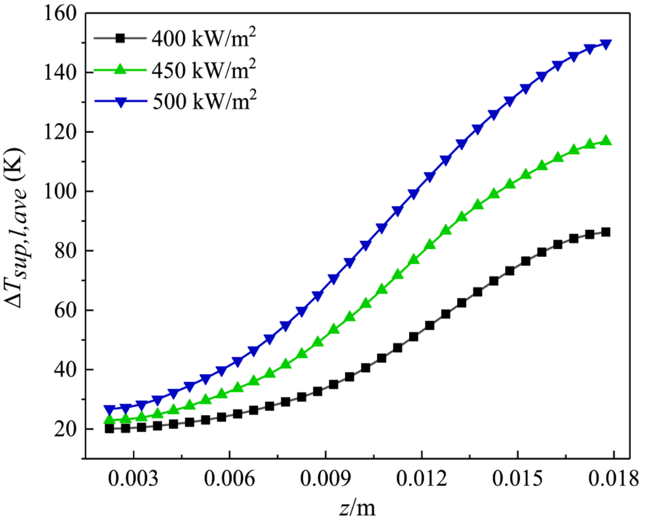

Fig. 7. Wall superheating profiles along the flow direction under the representative heat fluxes.

superheating gradient inside the wall along the flow direction increases with the heat flux. The average heat fluxes through the central section of the wall ($z = 0.01$ m) are 904.16, 1346.20, and 1729.42 kW/m^2 when the applied heat fluxes are 400, 450, and 500 kW/m^2, respectively. Fig. 8 displays the average heat flux profiles along the flow direction in the dynamically stable stage of the flow boiling. More heat in the dry patch region is conducted to the nucleate boiling region with the increase of heat flux, and it is brought away from there. Therefore, when the heat flux exceeds 400 kW/m^2, the wall superheating does not increase exponentially, and the reduction rate of HTC slows down slightly.

4.2.2. Quantitative analysis of local wall heat transfer characteristics

In this subsection, a quantitative analysis of local HTC and vapor fraction profiles along the flow direction under the representative heat fluxes are presented. The local HTC and vapor fraction near the inlet and outlet are neglected because no nucleation sites are put there. The local HTC is calculated by Eq. (32). As shown in Fig. 9, along the flow direction, the local HTC keeps growing for the case with a heat flux of 200 kW/m^2, while it increases at first and then decreases in other cases. As shown in Fig. 3, the bubbles coalesce with each other during the forward flowing, and its effect on heat transfer depends on whether large/elongated bubbles are formed with a large dry patch below. If not, the heat transfer is enhanced; otherwise, it worsens. Next, the reasons for the different trends of HTC are explained.

$$h_{local,ave} = \sum_{t}^{t+\Delta t} \frac{\sum_{i}^{N_{local}} q_i / N_{local}}{\left(T_{w,local} - T_{b,local}\right)} / \Delta t \tag{32}$$

where N_{local} expresses the node number for obtaining the local average heat flux.

When the heat flux is 200 kW/m^2, along the flow direction, the boiling intensity enhances with the slight increase of vapor fraction, leading to the continued rise of HTC. As the heat flux increases to 300 kW/m^2, the advantage of boiling enhancement is failed downstream because of the negative effects of the dry patch below some big slipping bubbles near the outlet, causing an inflection point ($z = 13.25$ mm) at the HTC curve. Besides, as shown in Fig. 10, a corresponding turning point can be found at the vapor fraction curve, implying the volume of the slipping bubble increases rapidly from this point. And it indirectly proves that the dry patch area is growing. Furthermore, as shown in Fig. 10, the vapor fraction increases rapidly from the upstream when the

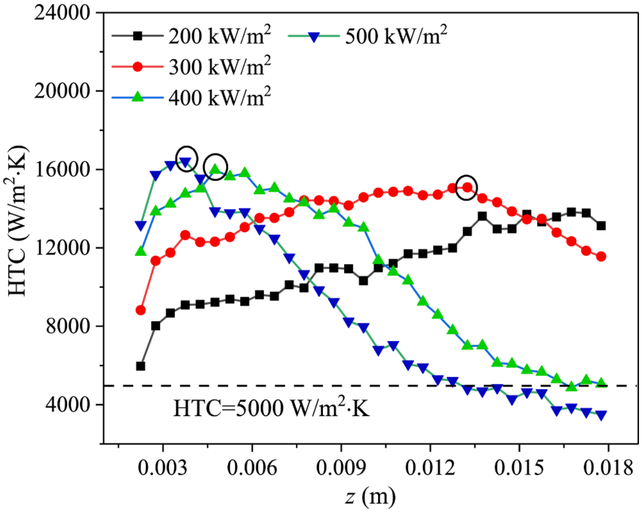

Fig. 9. Trends of HTC distributions along the flow direction under representative heat fluxes.

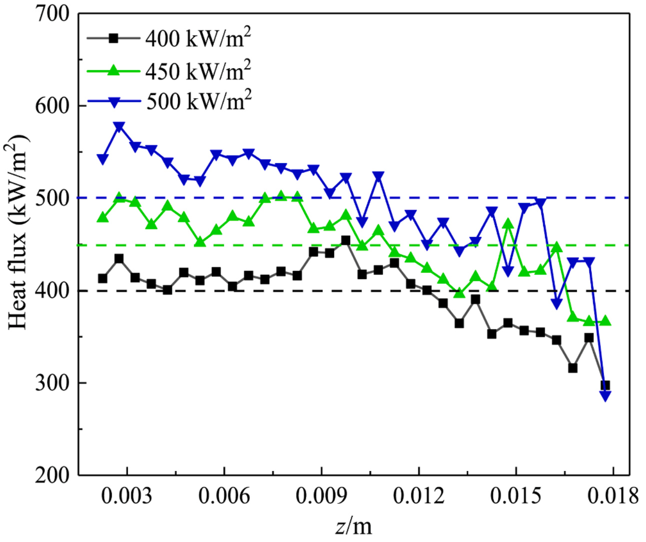

Fig. 8. Heat flux profiles along the flow direction under the representative heat fluxes.

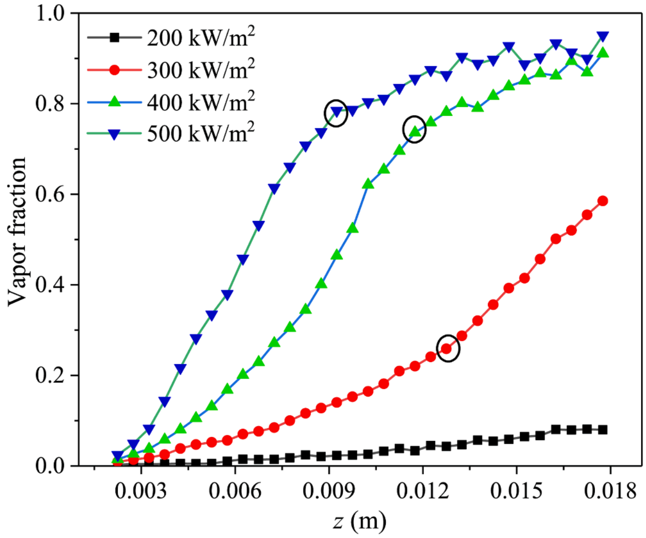

Fig. 10. Trends of vapor fraction distributions along the flow direction under representative heat fluxes.

heat flux exceeds 400 kW/m^2, indicating that the dry patch extends to the middle and upper reaches of the mini-channel, and the reflection point of the HTC curve moves towards the entrance as well. More importantly, the vapor fraction is over 0.8 from $z = 0.01025$ m to the outlet for the case with the heat flux of 500 kW/m^2, and the downstream is almost filled with elongated bubbles most of the time. The dry patch below these elongated bubbles causes the local HTC to be below 5000 W/m^2•K, which verified the occurrence of heat transfer deterioration and boiling crisis near the channel outlet from the perspective of local HTC.

4.2.3. Quantitative analysis of characteristic wall superheating curve

In this subsection, the last thing to highlight is to obtain the quantitative DNB and CHF of the subcooled flow boiling in the studied mini-channel. It is noteworthy that the maximum average wall superheating is 76.96 K when the heat flux is 500 kW/m^2, while the maximum local wall superheating is up to 183.04 K. The whole wall superheating is not out of control once local heat transfer deteriorates with a large dry patch. Therefore, in this study, the highest local wall superheating during flow boiling is selected as the characteristic wall superheating to obtain its relationship with the heat flux. As shown in Fig. 11, an obvious turning point at $q = 325$ kW/m^2 is observed in the characteristic wall superheating curve. After that, the characteristic wall superheating increases linearly with heat flux. However, there is no soaring phenomenon in the curve of characteristic wall superheating. On the premise of appearing local large-area dry patch, the main reasons for no soaring wall superheating rise are the periodic rewetting of the dry patch and the vertical heat conduction inside the solid wall.

Fig. 12 shows representative snapshots of subcooled flow boiling under the heat flux of 325 kW/m^2. For better presentation, the legend in Fig. 12 is different from that in Fig. 3. The slug flow happens with some elongated bubbles occupying the whole channel section near the outlet, and large dry patches below them are observed. Therefore, the formation of a large dry patch is the indicator of the quick increase of characteristic wall superheating. However, the characteristic wall superheating is only 45.23 K at $q = 325$ kW/m^2, and it is inappropriate to consider this value as the CHF. Besides, as shown in Fig. 12, nucleate boiling is inhibited due to the presence of elongated bubbles near the outlet. Therefore, in the present study, the heat flux of 325 kW/m^2 can be regarded as the point of DNB. The observation of this DNB is of great importance for the security of practical equipment operation.

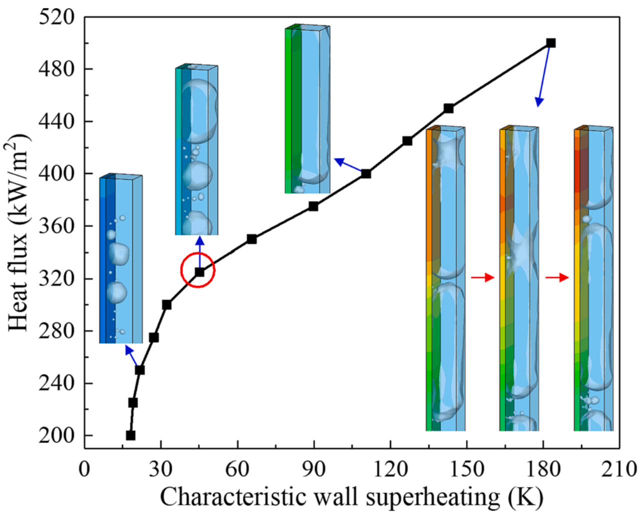

Fig. 11. Profile of characteristic wall superheating with heat flux.

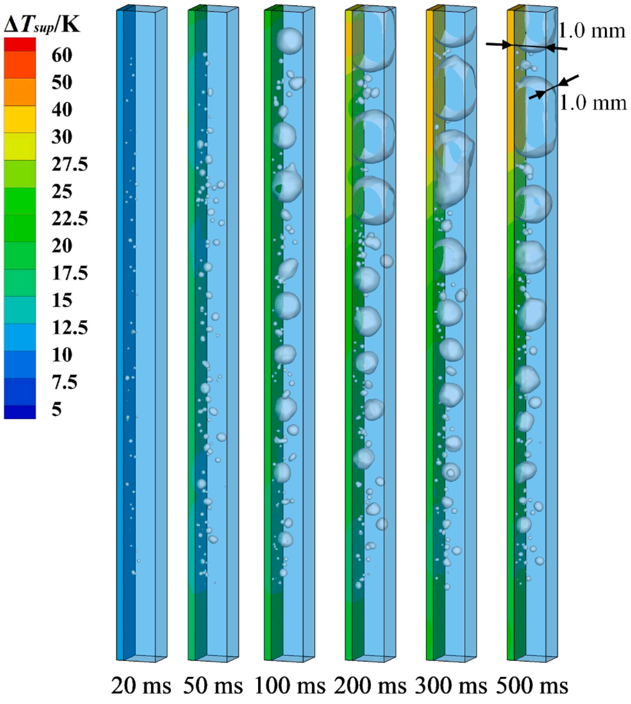

Fig. 12. Representative snapshots of 3D subcooled flow boiling under the heat flux of 325 kW/m^2.

In addition, the characteristic wall superheating increases linearly when the heat flux is over the DNB, leading to the difficulty in obtaining the CHF by its rising rate. Based on the above illustration and analyses, it can be concluded that the rapid increase in local wall superheating will happen once the region is covered by a large dry patch, which may trigger the boiling crisis. Therefore, during the dynamically stable stage of flow boiling, if the monotonous increment of local wall superheating exceeds 25 K in a short time under a certain heat flux, that can be regarded as the CHF. From representative snapshots of 3D subcooled flow boiling in Fig. 3, it is found that the high wall superheating tends to appear near the channel outlet. Therefore, the profile of local wall superheating with time in this region is used to identify the CHF. As shown in Fig. 13, the local wall superheating in the region near the channel outlet rises and falls periodically because of the periodic rewetting of dry patches. On the other hand, the area of dry patches is different, causing different changing amplitudes in local wall superheating. According to the defined triggering criterion of boiling crisis in

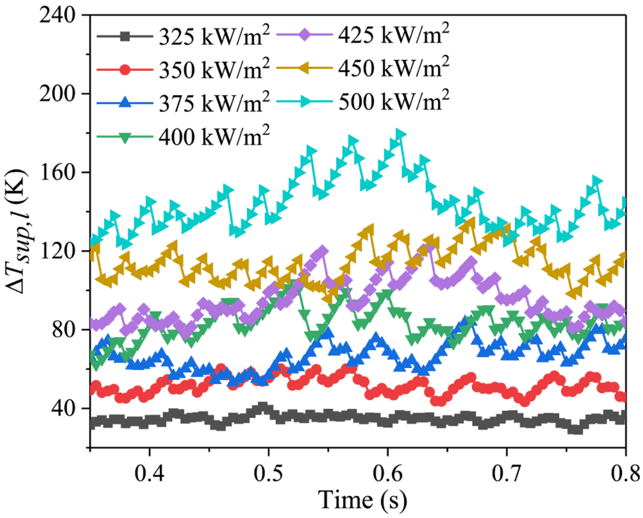

Fig. 13. Trends of local wall superheating near the channel outlet under different heat fluxes.

this study, the CHF of 375 kW/m^2 is obtained, and the corresponding local wall superheating increases monotonously from 58.53 to 84.00 K in the time range 0.63 to 0.67 s. Next, the triggering process is illustrated further by the bubble contours.

As displayed in Fig. 14, the length of isolated elongated bubbles is short at 620 ms, without obvious heat transfer deterioration. Then, some adjacent elongated bubbles near the channel outlet coalesce into a longer one at 625 ms, and some subsequent bubble merges into this long elongated bubble at 630, 635, and 640 ms. As a result, the large dry patch below the long elongated bubble requires much time to rewet, and the heat transfer in the vicinity of the channel outlet deteriorates, leading to a sharp rise of local wall superheating in a short time and triggering the flow boiling crisis. The defined triggering criterion of the boiling crisis in this study is unconventional. Therefore, no quantitative comparison is made in CHF between the present numerical simulation method and empirical correlations or experimental data.

In summary, quantitative analysis indicates that the HTC near the outlet keeps at a low level for the case with high heat flux because of the high vapor fraction with a large dry patch, which causes the heat transfer deterioration and boiling crisis even though much heat from the dry patch region is brought away by heat conduction inside solid wall. Besides, DNB (about 325 kW/m^2) and CHF (about 375 kW/m^2) are obtained by profiles of characteristic wall superheating and local wall superheating.

5. Conclusions

In this paper, the VOSET method is adopted to investigate the subcooled flow boiling and its crisis in a vertical rectangular mini-channel by considering conjugated heat transfer and a reasonable nucleation site density model. The evolution of bubble and flow patterns of subcooled flow boiling is reproduced. The small bubbles up to the quantity of 138 are accurately captured in the studied mini-channel within the heat fluxes of 500 kW/m^2. The relationship between flow pattern and heat transfer is discussed, and the triggering mechanism of the flow boiling crisis is revealed based on the formation and development of the dry patch. The major conclusions based on present simulation conditions are summarized as follows.

(1) The flow boiling crisis in the vertical rectangular mini-channel is triggered by a large dry patch. Once a large dry patch appears below the elongated bubble, the heat exchange between the liquid and heating wall is isolated. If the elongated bubble in the midstream keeps merging downstream, the dry patch near the outlet cannot be rewetted in a short time, and the wall temperature will increase sharply and trigger the boiling crisis. This triggering mechanism of the flow boiling crisis is new and different from the traditional ones. Besides, unlike pool boiling, much heat from the dry patch region is transferred to the nucleate boiling region by wall conduction, and the heat transfer deterioration is not easy to happen.

(2) A DNB point of the subcooled flow boiling in the studied vertical rectangular mini-channel is obtained based on the characteristic wall superheating. A distinct turning point at 325 kW/m^2 is found in the characteristic wall superheating curve when the elongated bubble forms with a large-area dry patch below it, which is defined as the DNB point because the wall superheating is not very high while nucleate boiling is inhibited. Beyond this point, the wall superheating increases much faster with heat flux.

(3) The characteristic wall superheating increases linearly when the heat flux is over the DNB, leading to the difficulty in obtaining the CHF by its rising rate. On the other hand, once a large dry patch covers one region, the sharp increase of local wall superheating with time will occur. Therefore, in this study, a new boiling crisis's triggering criterion is defined as the monotonous increment of local wall superheating is over 25 K in a short time, and a CHF of about 375 kW/m^2 is obtained based on that.

Declaration of Competing Interest

The authors declare that they have no known competing financial interests or personal relationships that could have appeared to influence

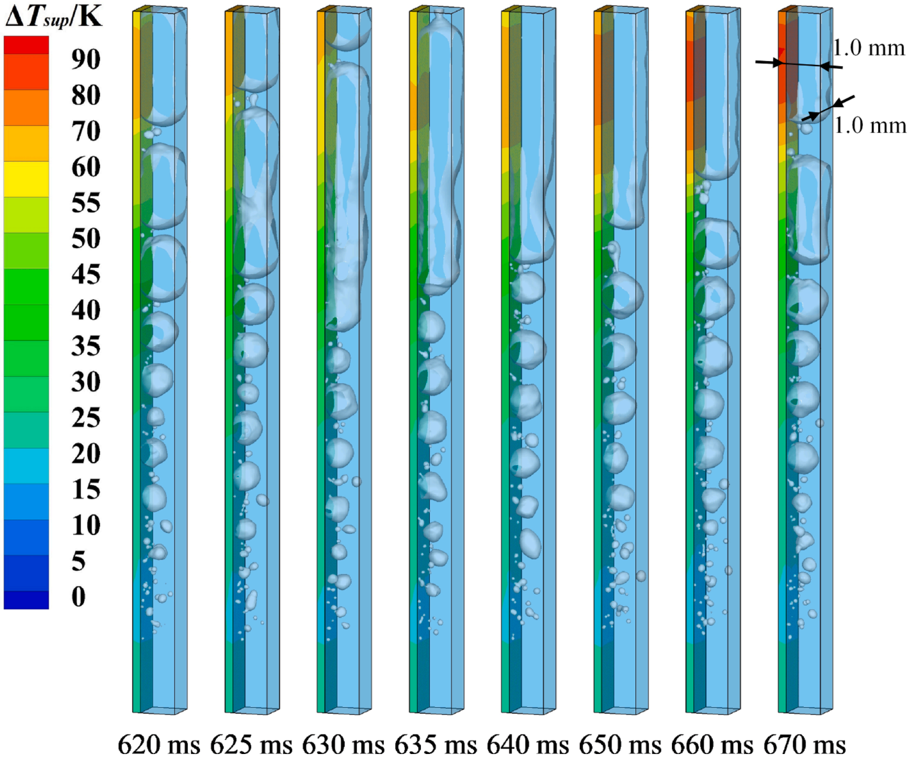

Fig. 14. Representative snapshots of 3D subcooled flow boiling under the heat flux of 375 kW/m^2.

the work reported in this paper.

Data availability

Data will be made available on request.

Acknowledgment

This work is supported by the Joint Funds of the National Natural Science Foundation of China (U2141218), the National Natural Science Foundation of China (52176150, 52076015), the Scientific Research Project of Beijing Educational Committee(KZ202110017026), the RETH Open Fund (2021RETHOF-241001), the Project for Young Talents of China National Nuclear Corporation, the Foundation for Innovative Research Groups of the National Natural Science Foundation of China (51721004), the Introducing Talents of Discipline to Universities (B16038), and the Award Cultivation Foundation from Beijing Institute of Petro-chemical Technology (BIPTACF-002).

References

[1] L. Cheng, G. Xia, Fundamental issues, mechanisms and models of flow boiling heat transfer in microscale channels, Int. J. Heat Mass Transf. 108 (2017) 97–127.

[2] X. Fang, Y. Yuan, A. Xu, L. Tian, Q. Wu, Review of correlations for subcooled flow boiling heat transfer and assessment of their applicability to water, Fusion Eng. Des. 122 (2017) 52–63.

[3] L.S. Tong, Boundary-layer analysis of the flow boiling crisis, Int. J. Heat Mass Transf. 11 (1968) 1208–1211.

[4] J. Weisman, B.S. Pei, Prediction of critical heat flux in flow boiling at low qualities, Int. J. Heat Mass Transf. 26 (1983) 1463–1477.

[5] C.H. Lee, I. Mudawwar, A mechanistic critical heat flux model for subcooled flow boiling based on local bulk flow conditions, Int. J. Multiph. Flow 14 (1988) 711–728.

[6] J.E. Galloway, I. Mudawar, CHF mechanism in flow boiling from a short heated wall-II. Theoretical CHF model, Int. J. Heat Mass Transf. 36 (1993) 2527–2540.

[7] W. Liu, H. Nariai, Ultrahigh CHF prediction for subcooled flow boiling based on homogenous nucleation mechanism, ASME Journal of Heat Transfer 127 (2005) 149–158.

[8] S.J. Ha, H.C. No, A dry-spot model of critical heat flux in pool and forced convection boiling, Int. J. Heat Mass Transf. 41 (1998) 303–311.

[9] S.H. Kim, I.C. Chu, M.H. Choi, D.J. Euh, Mechanism study of departure of nucleate boiling on forced convective channel flow boiling, Int. J. Heat Mass Transf. 126 (2018) 1049–1058.

[10] K. Hata, K. Fukuda, S. Masuzaki, Mechanism of critical heat flux during flow boiling of subcooled water in a circular tube at high liquid Reynolds number, Exp. Therm Fluid Sci. 70 (2016) 255–269.

[11] Y. Sato, B. Niceno, Pool boiling simulation using an interface tracking method: From nucleate boiling to film boiling regime through critical heat flux, Int. J. Heat Mass Transf. 125 (2018) 876–890.

[12] K. DolatiAsl, Y. Bakhshan, E. Abedini, S. Niazi, Numerical investigation of critical heat flux in subcooled flow boiling of nanofluids, J. Therm. Anal. Calorim. 139 (2019) 2295–2308.

[13] R. Zhang, T. Cong, G. Su, J. Wang, S. Qiu, Investigation on the critical heat flux in typical 5 by 5 rod bundle at conditions prototypical of PWR based on CFD methodology, Appl. Therm. Eng. 179 (2020).

[14] H. Pothukuchi, S. Kelm, B.S.V. Patnaik, B.V.S.S.S. Prasad, H.J. Allelein, CFD modeling of critical heat flux in flow boiling: validation and assessment of closure models, Appl. Therm. Eng. 150 (2019) 651–665.

[15] S. Osher, J.A. Sethian, Fronts propagating with curvature dependent speed: algorithms based on Hamilton-Jacobi formulations, J. Comput. Phys. 79 (1988) 12–49.

[16] C.W. Hirt, B.D. Nichols, Volume of fluid (VOF) method for the dynamics of free boundary, J. Comput. Phys. 39 (1981) 201–225.

[17] D. Sun, W.Q. Tao, A coupled volume-of-fluid and level set (VOSET) method for computing incompressible two-phase flows, Int. J. Heat Mass Transf. 53 (2010) 645–655.

[18] A. Mukherjee, S.G. Kandlikar, Numerical simulation of growth of a vapor bubble during flow boiling of water in a microchannel, Microfluid. Nanofluid. 1 (2005) 137–145.

[19] A. Mukherjee, S.G. Kandlikar, Numerical study of single bubbles with dynamic contact angle during nucleate pool boiling, Int. J. Heat Mass Transf. 50 (2007) 127–138.

[20] J. Lee, G. Son, Numerical simulation of conjugate heat transfer and bubble motion in subcooled flow boiling, J. Mech. Sci. Technol. 29 (2015) 1815–1821.

[21] W. Lee, G. Son, H.Y. Yoon, Direct numerical simulation of flow boiling in a finned microchannel, Int. Commun. Heat Mass Transfer 39 (2012) 1460–1466.

[22] Y.Q. Zu, Y.Y. Yan, S. Gedupudi, T.G. Karayiannis, D.B.R. Kenning, Confined bubble growth during flow boiling in a mini-/micro-channel of rectangular cross-section part II: approximate 3-D numerical simulation, Int. J. Therm. Sci. 50 (2011) 267–273.

[23] Y. Luo, W. Li, K. Zhou, K. Sheng, S. Shao, Z. Zhang, J. Du, W.J. Minkowycz, Three-dimensional numerical simulation of saturated annular flow boiling in a narrow rectangular microchannel, Int. J. Heat Mass Transf. 149 (2020), 119246.

[24] K. Ling, G. Son, D. Sun, W. Tao, Three dimensional numerical simulation on bubble growth and merger in microchannel boiling flow, Int. J. Therm. Sci. 98 (2015) 135–147.

[25] K. Ling, S. Zhang, W. Liu, X. Sui, W. Tao, Interface tracking simulation for subcooled flow boiling using VOSET method, Front. Energy Res. 8 (2021), 526035.

[26] J. Smagorinsky, General circulation experiments with the primitive equations, Mon. Weather Rev. 91 (1963) 99–164.

[27] M.M. Francois, S.J. Cummins, E.D. Dendy, D.B. Kothe, J.M. Sicilian, M. W. Williams, A balanced-force algorithm for continuous and sharp interfacial surface tension models within a volume tracking framework, J. Comput. Phys. 213 (2006) 141–173.

[28] F. Gibou, L. Chen, D. Nguyen, S. Banerjee, A level set based sharp interface method for the multiphase incompressible Navier-Stokes equations with phase change, J. Comput. Phys. 222 (2007) 536–555.

[29] K. Ling, Z. Li, D. Sun, Y. He, W. Tao, A three-dimensional volume of fluid & level set (VOSET) method for incompressible two-phase flow, Comput. Fluids 118 (2015) 293–304.

[30] Q. Li, Y. Jiao, M. Avramova, P. Chen, J. Yu, J. Chen, J. Hou, Development, verification and application of a new model for active nucleation site density in boiling systems, Nucl. Eng. Des. 328 (2018) 1–9.

[31] M.M. Shah, A general correlation for heat transfer during subcooled boiling in pipes and annuli, ASHRAE Trans. 93 (1977) 202–217.

[32] T.L. Bergman, A.S. Lavine, F.P. Incropera, D.P. DeWitt, Introduction to heat transfer, 6th Edition, John Wiley & Sons, New York, 2011.

[33] S.S. Papell, Subcooled boiling heat transfer under forced convection in a heated tube, Lewis Research Center, Cleveland, 1963.

[34] K.E. Gungor, R.H.S. Wintertion, A general correlation for flow boiling in tubes and annuli, Int. J. Heat Mass Transf. 29 (1986) 351–358.

[35] M.G. Cooper, Heat flow rates in saturated nucleate pool boiling-a wide-ranging examination using reduced properties, Adv. Heat Tran. 16 (1984) 157–239.

[36] Z. Liu, R.H.S. Winterton, A general correlation for saturated and subcooled flow boiling in tubes and annuli, based on a nucleate pool boiling equation 34 (1991) 2759–2766.

[37] S.S. Kutateladze, Boiling heat transfer, Int. J. Heat Mass Transf. 4 (1961) 31–45.